COSMIC RAY EFFECTS INDUCED IN A ROCK EXPOSED ON THE MOON OR IN FREE SPACE: CONTRAST IN PATTERNS FOR 'TRACKS' AND 'ISOTOPES'*

S. K. BHATTACHARYA, J. N. GOSWAMI, S. K. GUPTA, and D. LAL

*Tata Institute of Fundamental Research, Bombay, India and
Physical Research Laboratory, Ahmedabad, India*

Abstract. Analytical studies are reported here for two cosmogenic effects due to low energy particles in extraterrestrial samples:

(i) Formation of latent chemically etchable tracks in crystalline materials due to solid state damage as a result of ionisation losses suffered by multicharged cosmic ray nuclei, and

(ii) Production of low threshold isotopes due to nuclear interactions of solar cosmic ray particles.

The present analytical treatment is different from those previously reported and is more directly applicable to recent studies of low energy cosmogenic effects in meteorites and in lunar samples. We consider irradiation of ellipsoidal rocks in space and on the Moon. In the latter case, different irradiation geometries corresponding to different burials in the regolith are also considered.

It is shown that results of irradiation of an object on the surface of a parent body differ from that of an object in free space in more complex manner than a uniform reduction by a factor of two due to the change over from 2π to 4π irradiation. Isocontours for 'tracks' or 'isotopes' are found to be markedly different in the two cases. Thus, the irradiation geometry must be explicitly taken into account in interpreting low-energy cosmogenic effects in lunar rocks. Simultaneous analyses of tracks and radioisotopes of different half-lives should allow one to establish principal irradiation geometries both for meteorites and lunar samples.

1. Introduction

It is now well known that the irradiation history of meteorites can usually be represented by an exposure in space after some collisional event leading to the dislodging of objects of varying sizes from a parent body. Thus, the outer layers of the meteorite contain records of low-energy particle irradiation. However, the process of terrestrial capture often involves an appreciable ablation and mass-wastage (during entry through the Earth's atmosphere) with the result that the low energy particle record is usually obliterated. There is an exception to this general statement and this relates to the preservation of single grains irradiated by cosmic rays in space which later become part of a large body due to compaction/aggregation (Lal and Rajan, 1969; Pellas *et al.*, 1969). Thus, in some cases a well preserved low energy record can be found within a meteorite. In favourable cases atmospheric ablation can be very small, for example, due to an oriented entry of the meteorite without tumbling (Price *et al.*, 1967; Lal *et al.*, 1969; Bhandari *et al.*, 1973). Meteorites indicated as having small ablation have been studied for low energy cosmic ray particle induced effects –

---

* Paper dedicated to Prof. Harold C. Urey on the occasion of his 80th birthday on 29 April 1973.

radioactivity due to solar cosmic rays (Amin *et al.*, 1969) and fossil tracks due to cosmic ray multicharged nuclei (Price *et al.*, 1967; Lal *et al.*, 1969).

Until July 1969, meteorites were the only extraterrestrial objects available for studying the history of cosmic rays in space. In subsequent months the situation changed drastically with the availability of lunar samples where low energy cosmic irradiation history is preserved undisturbed. Consequently, the scope of studying the history of low energy cosmic ray particles, in particular, has increased manifold. Several clearcut examples of low energy particle induced effects were seen in the very first batch of lunar samples analysed (Crozaz *et al.*, 1970; Fleischer *et al.*, 1970; Lal *et al.*, 1970; Price and O'Sullivan, 1970; Shedlovsky *et al.*, 1970). But at the same time, the geometry and irradiation history of lunar samples are more complex. This necessitates a very detailed analysis of cosmogenic effects in the rocks. In view of this consideration, we present here detailed calculations of low energy effects for:

(i) the formation rates of latent chemically etchable tracks due to solar and galactic cosmic ray multicharged nuclei within spherical and ellipsoidal rocks of different sizes, both for their exposure in free space and on the surface of a parent body with different irradiation geometries as encountered in the case of lunar rocks,

(ii) the production rates of certain low threshold radioisotopes due to solar cosmic radiation for different irradiation geometries as discussed above.

The analytical data presented herein became necessary with the availability of lunar samples. The lunar missions and the present world interest in the Moon is largely due to the intellectual inquiry of the Moon to which Prof. Harold Urey has contributed a great deal: this paper is dedicated to him on the occasion of his eightieth birthday.

2. Rate of Registration of Etchable Tracks in Centimeter-size Objects: 4π and 2π Irradiation Geometries

We will base our calculations on the over-simplified track registration model adopted by Fleischer *et al.* (1967). It is assumed that etchable tracks are registered within a range of energies where the solid state damage exceeds a certain value; this interval of energy of course depends on the atomic number Z of the ion and the detector characteristics.

2.1. GENERAL ANALYTICAL EXPRESSION FOR TRACK REGISTRATION RATE

In this section we shall briefly summarize the analytical expressions and the parameters which enter in the calculation of the rate of registration (i.e. formation) of nuclear tracks due to multicharged cosmic ray nuclei. The first analytical expression for the rate of track formation in a spherical object exposed in space was given by Fleischer *et al.* (1967). Expected track formation rates for a variety of spectral shapes for the cosmic ray nuclei were subsequently discussed by Lal *et al.*, (1969) and Maurette *et al.* (1969). The latter authors also discussed in detail the expected angular distribution of tracks in a spherical object exposed in space. In the present

work we will consider the specific cases of track production corresponding to spherical and ellipsoidal rocks exposed either in free space or on parent body.

A general expression for the rate of track formation, $(\dot\varrho)_{z,x} = (d\varrho/dt)_{z,x}$ due to the group of nuclei of atomic numbers lying between Z and Z' at a depth X within an object can be written as

$$(\dot\varrho)_{z,x} = \sum_{i=1}^{n} \int_{\theta} \int_{\phi} \left[\frac{dN}{dE}\frac{dE}{dS}\right]_{X_i} \frac{\Delta R(Z)}{n} \exp(-\lambda X_i)\, F(Z \to Z', X_i) \times$$
$$\times |\cos\alpha|\, \sin\theta\, d\theta\, d\phi, \qquad (1)$$

where X_i is a function of $r(\theta, \phi)$, the penetration distance of an incoming particle in the rock.

$$X_i = r(\theta, \phi) + i(\Delta R(Z)/n). \qquad (2)$$

The symbols in Equations (1) and (2) are explained below:

(dN/dE) is the kinetic energy differential spectrum of cosmic ray primary nuclei of atomic number Z.

(dE/dS) is the slope of the range-energy curve for the nuclei in the detector material.

$[(dN/dE)(dE/dS)]_{X_i}$ is the differential flux $(\text{cm}^{-2}\,\text{s}^{-1}\,\text{sr}^{-1})$ of particles having a range X_i.

$\Delta R(Z)$ is the mean effective recordable track length for the group of nuclei of atomic number lying between Z and Z'

λ is the total nuclear interaction probability for nuclei of atomic number Z in the target material. (Since the difference between Z and Z' is small, a single value of λ is used in the calculations).

$F(Z \to Z', X_i)$ is the fragmentation factor to take into account the production of secondary nuclei of atomic numbers lying between Z and Z'.

The trigonometrical functions in Equation (1) represent the geometrical factors and will be discussed later for exposure in free space and on the Moon.

Equation (1) holds even when the differential flux at the detector is variable within the penetration distance interval $r(\theta, \phi)$ and $r(\theta, \phi) + \Delta R(Z)$ – a case which corresponds to track production in the near surface region of objects exposed in free space or on a parent body. In such cases the total flux in the direction (θ, ϕ) is obtained by summing the flux in 'n' steps where 'n' is suitably chosen to take into consideration the steepness of the energy spectrum in the relevant energy region. When the distance between the detector and the surface is very large compared to $\Delta R(Z)$, we can assume that the flux of particles is essentially constant over the small interval $\Delta R(Z)$ and Equation (1) then simplifies to

$$(\dot\varrho)_{z,x} = \int_{\theta}\int_{\phi} \left[\frac{dN}{dE}\frac{dE}{dS}\right]_{r(\theta,\phi)} \Delta R(Z) \exp(-\lambda r(\theta, \phi)) \times$$
$$\times F(Z \to Z', r(\theta, \phi))\, |\cos\alpha|\, \sin\theta\, d\theta\, d\phi. \qquad (3)$$

The range-energy (E vs S) relation, the interaction probability λ and the fragmentation parameter $F(Z \rightarrow Z', r(\theta, \phi)$ for different nuclei in targets of different compositions are discussed in Appendices I and II.

We will now discuss the geometrical factors entering in Equation (1) with reference to irradiation geometries in free space and on a parent body.

2.2. CASE OF EXPOSURE OF SPHERICAL AND ELLIPSOIDAL OBJECTS IN FREE SPACE

For a spherical rock of radius R, exposed in space, it is enought to calculate the track production rate along any one radial direction because of symmetry. If the detector is situated at a point A at a distance $X(=SA)$ from the nearest surface S, (see Figure 1), the distance $r(\theta, \phi)$ $(=QA)$ traversed by a particle in a direction (θ, ϕ) inside the body before reaching the detector is given by the following expression

$$r(\theta, \phi) = - (R - X) \cos \theta + [R^2 \cos^2 \theta + 2RX \sin^2 \theta - X^2 \sin^2 \theta]^{1/2}.$$
(4)

We note that in this case $r(\theta, \phi)$ is independent of angle ϕ because of symmetry.

As was pointed out earlier by Fleischer *et al.* (1967), the rate of track formation on a given detector surface depends on its orientation within the body. Two con-
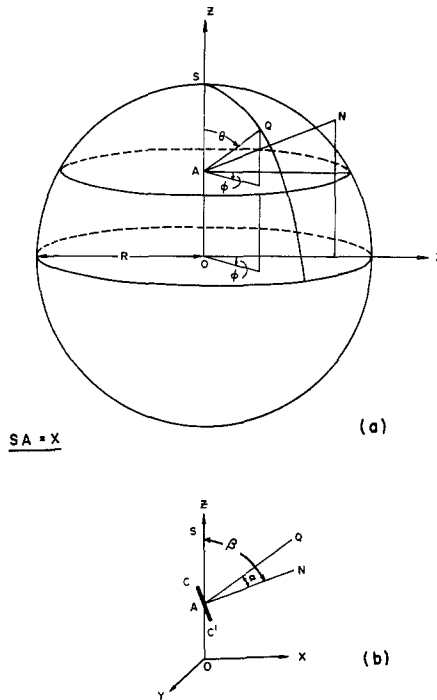

Fig. 1. Exposure geometry and the coordinate system for 4π irradiation of a spherical object, i.e. exposure in free space, is shown in Figure 1a. The orientation of the crystal plane (CC′) is uniquely defined by the angle β between the crystal normal and the radial direction through the crystal, as shown in Figure 1b. θ and ϕ refer to the direction of the incoming particle.

venient angles defining the detector orientation with respect to the particle direction and the nearest surface point respectively are α and β, and are defined below.

$\alpha = \angle\, QAN$, is the angle between the normal to the crystal plane AN and the particle direction QA.

$\beta = \angle\, SAN$, the angle between the normal to the crystal plane AN and the radial direction through the detector (see Figure 1).

The value of $\cos\alpha$ in Equation (3) is then given by:

$$\cos\alpha = \cos\theta\cos\beta + \sin\theta\sin\beta\cos\phi. \tag{5}$$

For the case of 4π irradiation, the normal to the crystal plan AN can be taken as lying in the X-Z plane without any loss of generality.

Equation (3) simplifies in particular cases when the angle β is 0 or $\pi/2$:

(a) when $\beta = 0$, i.e., the crystal plane is perpendicular to the radial direction through the detector,

$$\cos\alpha = \cos\theta; \text{ and}$$

$$(\dot{\varrho})_{Z,\,X;\,\beta=0} = 2\pi \int_0^\pi \left[\frac{dN}{dE}\frac{dE}{dS}\right]_{r(\theta)} \varDelta R(Z)\exp\left(-\lambda r(\theta)\right) \times$$
$$\times F\left(Z \to Z', r(\theta)\right) |\cos\theta| \sin\theta\, d\theta \tag{6}$$

(b) when $\beta = \pi/2$, i.e. the radial direction lies in the crystal plane,

$$\cos\alpha = \sin\theta\cos\phi$$

and

$$(\dot{\varrho})_{Z,\,X;\,\beta=\pi/2} = 4 \int_0^\pi \left[\frac{dN}{dE}\frac{dE}{dS}\right]_{r(\theta)} \varDelta R(Z)\exp\left(-\lambda r(\theta)\right) \times$$
$$\times F\left(Z \to Z', r(\theta)\right) \sin^2\theta\, d\theta. \tag{7}$$
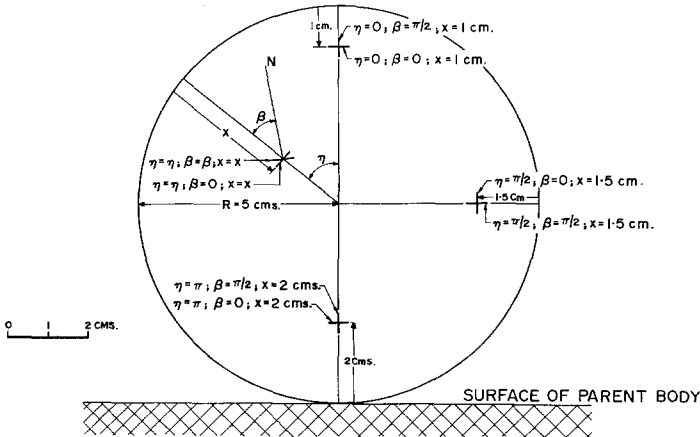

Fig. 2.   Illustrative orientations and positions of the crystal plane inside a spherical object on the surface of a parent body in terms of the angle variables η and β and distance X from the nearest surface.

S. K. BHATTACHARYA ET AL.

In the case of an ellipsoidal body the absence of spherical symmetry necessitates the specification of two more angles η and ζ, the zenith and the azimuth angles of the radial direction throught the crystal (Figure 4), respectively. The crystal position, A is uniquely specified by angles η, ζ and the depth, X measured from the nearest surface (see Figure 2). The distance $r(\theta, \phi)$ for this case is given in Appendix III. Using the given expression for $r(\theta, \phi)$, the track production rate can be calculated with the help of Equation (3).

2.3. CASE OF EXPOSURE OF SPHERICAL AND ELLIPSOIDAL OBJECTS ON A PARENT BODY

The calculation of the track densities for a rock shielded on one side (2π shielding), for instance, exposed on the lunar surface, becomes much more involved than for the case of a rock exposed in space. The complete rotational symmetry about the center is absent. But in the case of spherical rocks, the presence of a rotational symmetry about the zenith suggests that it is sufficient to calculate the track production rate only for points lying in a vertical cross-section through the center of the rock. This implies that the sample position has to be specified by two coordinates η and X (see Figure 2). In order to calculate the track production rate for different detector
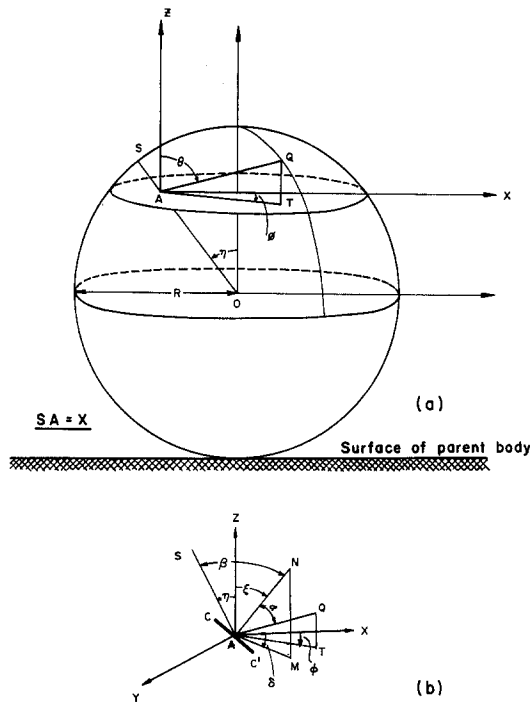

Fig. 3. Exposure geometry and the coordinate system for 2π irradiation of a spherical object, e.g. exposure on lunar surface is shown in Figure 3a. For a given η direction the orientation of the crystal plane (CC') is uniquely defined by the angles ζ and δ as shown in Figure 3b. The incoming particle makes an angle α w.r.t. to the crystal normal. β is the angle between the crystal normal and the radial direction through the crystal.

orientations, one has to, in addition to specifying the two angles β and η as previously defined, also specify two other angles ξ and δ to fix the orientation of the normal to the crystal place (see Figure 3). Further, the upper limit of θ integral in Equation (3) now becomes $\pi/2$ because when θ exceeds this value the parent body acts as a shield.

Considering the points discussed above, the track production rate $(\dot{\varrho})_{Z, X}$ which is a function of ξ, η and δ is given by

$$(\dot{\varrho})_{Z, X} = \int_{\phi=0}^{2\pi} \int_{\theta=0}^{\pi/2} \left[\frac{dN}{dE} \frac{dE}{dS} \right]_{r(\theta, \phi)} \Delta R(Z) \exp\left(-\lambda r(\theta, \phi)\right) \times$$
$$\times F\left(Z \rightarrow Z', r(\theta, \phi)\right) |\cos\alpha| \sin\theta \, d\theta \, d\phi. \quad (8)$$

The absolute value of $r(\theta, \phi)$ is given by

$$r(\theta, \phi) = -(R - X)\cos\gamma + \left[R^2 \cos\gamma + 2RX \sin^2\gamma - X^2 \sin^2\gamma\right]^{1/2}, \quad (9)$$

where γ is the angle between the particle direction, QA, and the radial direction of the sample position, OS (see Figure 3). Cosines of α, β and γ are related to other angles ξ, η, δ, θ and ϕ by the relations

$$\cos\alpha = \cos\xi \cos\theta + \sin\xi \cos\delta \sin\theta \cos\phi + \sin\xi \sin\delta \sin\theta \sin\phi, \quad (10a)$$

$$\cos\beta = \cos\xi \cos\eta - \sin\xi \cos\delta \sin\eta, \quad (10b)$$

$$\cos\gamma = \cos\theta \cos\eta - \sin\theta \sin\eta \cos\phi. \quad (10c)$$

In the special case, when $\eta = 0$: $\cos\gamma = \cos\theta$, i.e. for track registration along a vertical direction passing through the center of the rock, the expression for $r(\theta, \phi)$ becomes independent of ϕ and is the same as given in Equation (4).

We will now consider the case of exposure of an ellipsoidal rock on the surface of a parent body. Here we will consider two cases:

(i) Rock is lying flush on the lunar surface i.e. with no part buried under the regolith.

(ii) Part of the rock is buried.

For these cases, the particle penetration distance, $r(\theta, \phi)$, has been calculated and the results are given in Appendix III. The coordinate system used and the geometry of irradiation are shown in Figures 4 and 5 respectively.

The expression for track production rate for an ellipsoidal rock lying on the regolith is the same as Equation (8), but that for a partially buried rock is different and is given in Appendix IV.

2.4. RESULTS OF CALCULATION OF TRACK REGISTRATION RATES OF 4π AND 2π IRRADIA- TION GEOMETRIES

We have discussed above the analytical expressions for track formation rate and now we will present calculations for certain assumed spectral forms for iron group nuclei considering the contemporary cosmic ray data. We will consider only the simple case of spherical objects.
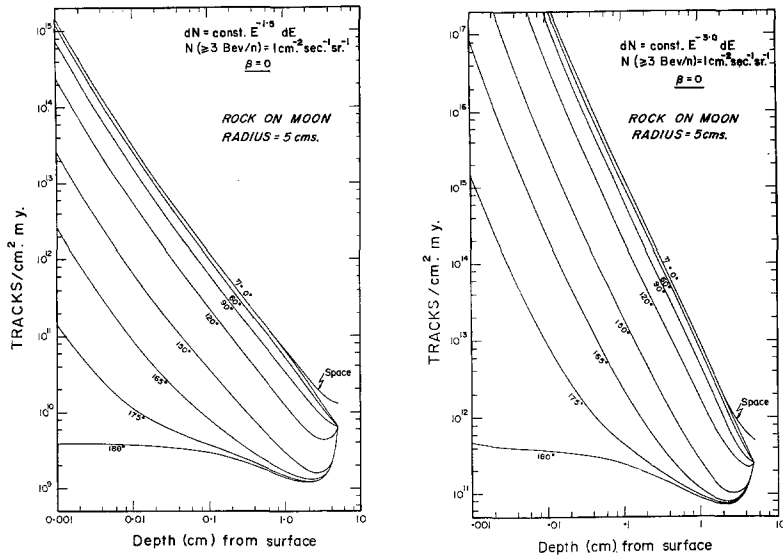
Fig. 4.   Exposure geometry and the coordinate system for 2π irradiation of an ellipsoidal body.
ζ is the azimuth angle of the radial direction through the crystal.

Fig. 5.   Exposure geometry and the coordinate system for 2π irradiation of a partially buried
ellipsoidal body. For given η, ζ and ϕ, θ_c refers to zenith angle of the rim of unburied cap w.r.t. the
crystal position A.

Fig. 6. Calculated track production rates ($\dot{\varrho}$) plotted as a function of depth for various zenith angles η, for a rock of radius of 5 cm irradiated in 2π and 4π geometries. All values are for $\beta = 0$ crystal orientation and a kinetic energy power law spectrum: $dN = $ const $E^{-\gamma} dE$. The two figures are for $\gamma = 1.5$ and 3.0, in each case normalising the constant by taking $N(\geqslant 3 \text{ BeV}) = 1$ particle cm^{-2} s^{-1} sr^{-1}. *Note* that in each case, the distance is measured from the nearest point of the rock surface, which is η dependent (see Figure 2).
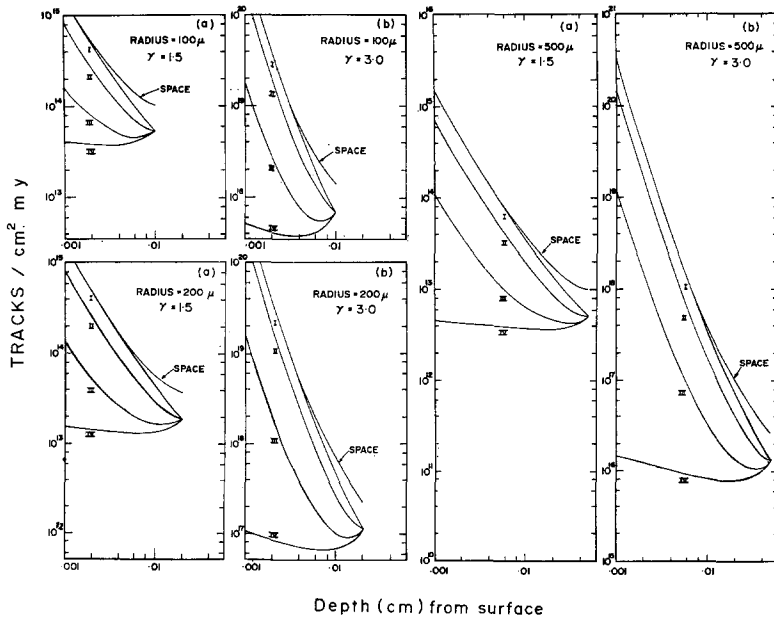

Fig. 7. Calculated track production rates ($\dot{\varrho}$) as in Figure 6, for spherical grains of radius 100μ, 200μ and 500μ irradiated in 2π and 4π geometries. Profiles labelled I, II, III and IV correspond to $\eta = 0°$, $90°$, $135°$ and $180°$ respectively.

The spectral form for the kinetic energy spectra of the primary Fe group (VH) nuclei in cosmic radiation is often well represented by the power law

$$dN = \text{const.}\, E^{-\gamma}\, dE, \tag{11}$$

with values of γ, between 1.5 and 3.0.

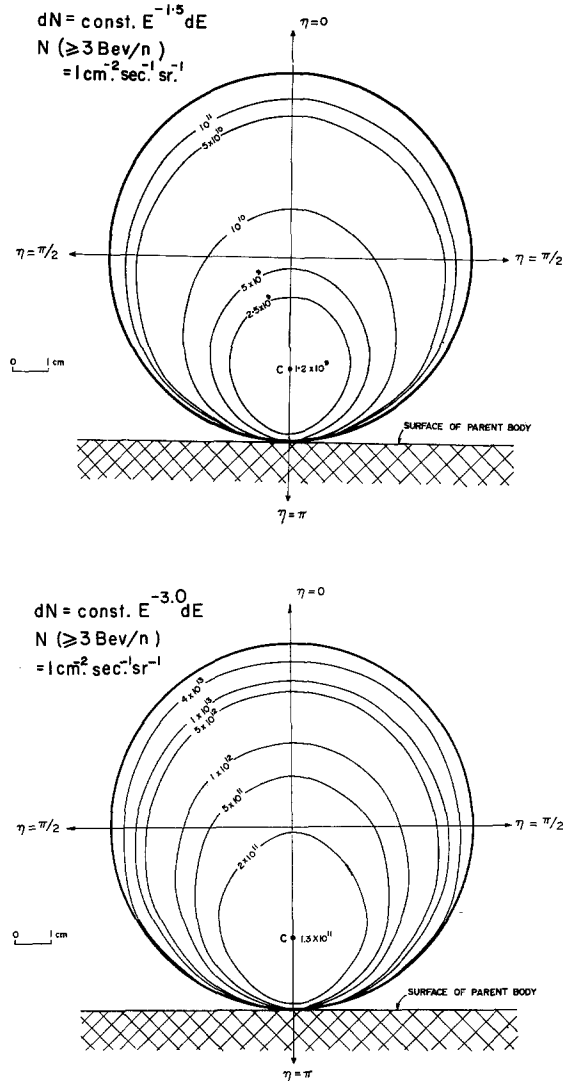Calculated production rates for spherical rocks of different radii are presented in

Fig. 8.   Iso-track production contours in a vertical diametral plane for $\beta = 0$ crystal orientation in 2π irradiation geometry of a spherical rock of radius 5 cm. A kinetic energy power law spectrum, $dN = \text{const}\, E^{-\gamma}\, dE$ has been assumed. The two figures are for $\gamma = 1.5$ and 3.0.

Figs. 6 to 11 based on the kinetic energy power law spectrum (Equation 11), normalising the constant so that

$$N_{(\geqslant 3 \text{ BeV})} = 1 \text{ particle cm}^{-2} \text{ s}^{-1} \text{ sr}^{-1}.$$

In Figure 6 track production rates are presented for a rock of radius 5 cm, exposed unburied (see Figure 3) on the surface of a parent body for $\beta = 0$ orientation of the crystal, as a function of depth for different zenith angles η for the spectral exponent $\gamma = 1.5$ and 3.0 respectively. In these figures we have also presented the expected track production rates for irradiation in free space, to allow comparison.

Similar calculations as in Figure 6 are shown for small sized spherical grains of radius 100 μ, 200 μ, and 500 μ for 2π and 4π irradiation geometries in Figure 7.
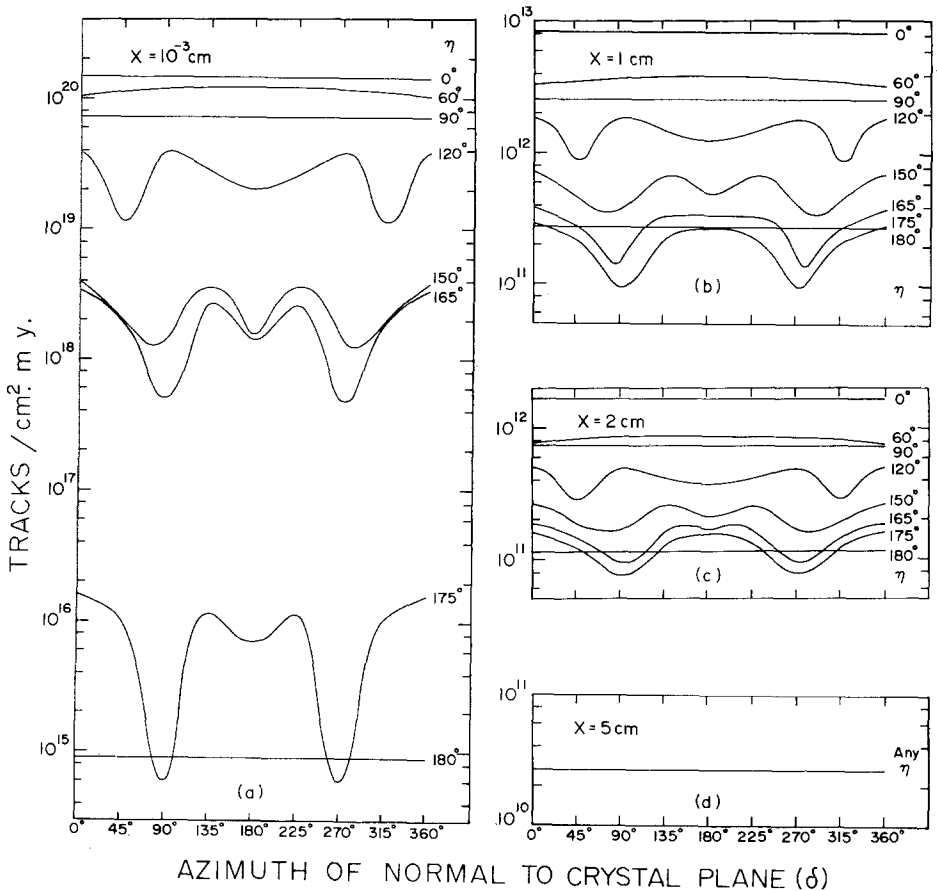

Fig. 9.   Track production rates for 2π irradiation geometry is given as a function of the azimuth angle δ of the normal to the crystal plane for different zenith angles η. The values are for $\beta = \pi/2$ orientation of the crystal inside a body of radius 5 cm. Calculations are shown for depth $X = 10\mu$, 1 cm, 2 cm and 5 cm measured from the nearest surface point. The calculations are for kinetic energy power law spectrum with the exponent $\gamma = 3.0$.
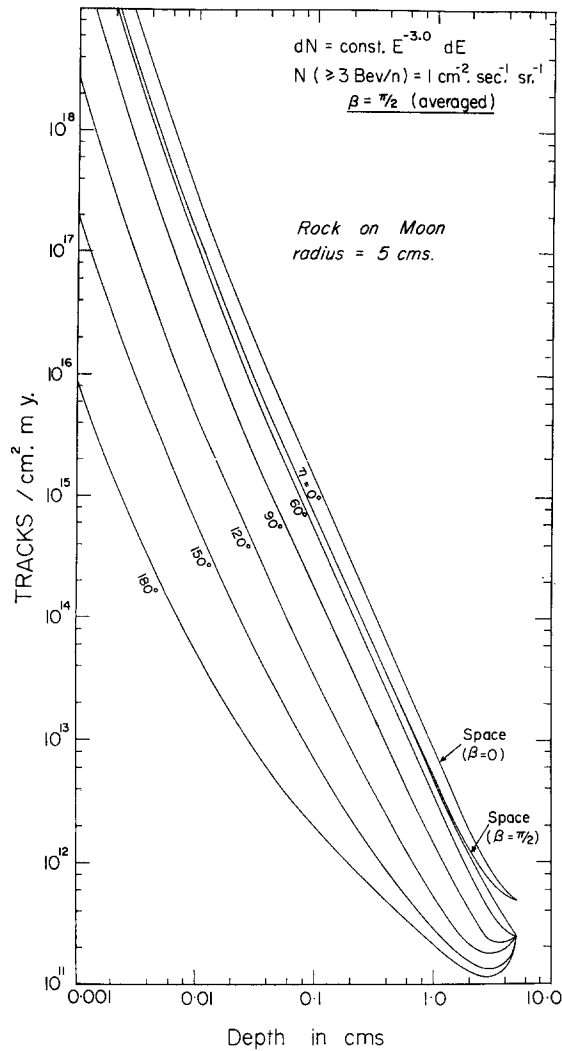
Fig. 10. Calcluated track production rates for $\beta = \pi/2$ orientation of the crystal as a function of depth for various zenith angles η in 2π irradiation geometry for a rock of radius 5 cm. Distances are measured from the nearest surface point. A kinetic energy power law spectrum with exponent $\gamma = 3.0$ has been used. Note that when $\beta \neq 0$, the track production rate in 2π irradiation geometry is a function of the angle δ (see Figure 9). The results shown in this figure are averages over the angle δ.

The iso-track production contours for a rock of radius 5 cm exposed unburied on a parent body are shown in Figure 8 for two different spectral forms as considered above.

In Figure 9 we have shown the calculated track densities at depths $10\ \mu$, 1 cm, 2 cm and center for the case of a rock of 5 cm radius exposed unburied (see Figure 3) on a parent body for $\beta = \pi/2$ orientation of the crystal as a function of δ, the azimuth angle of the normal to the detector plane, for a set of η values. The δ-averaged track production rate for this case (i.e. $\beta = \pi/2$, radius = 5 cm) as a function of depth for
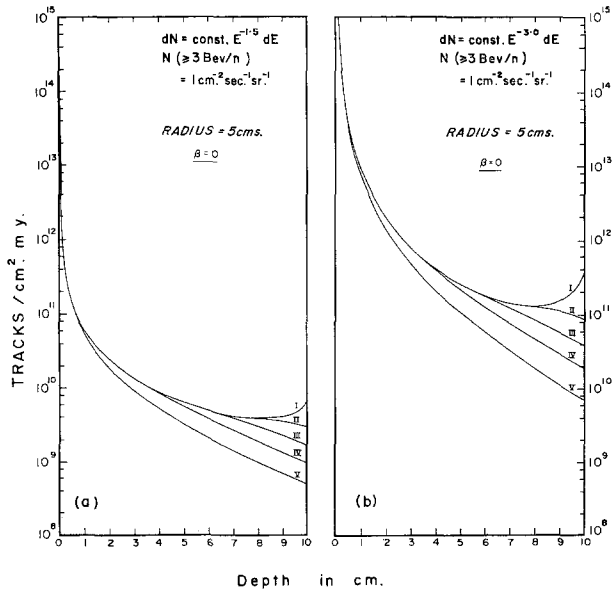
Fig. 11. Calculated track production rates for $\eta = 0$ as a function of depth for a spherical rock of 5 cm with partial and complete burial. Track profile I is for no burial; II, III, IV and V refer to burial of 2.5, 5.0, 7.5 and 10 cm respectively. (Profile V corresponds to the case of complete burial). The crystal orientation is taken as $\beta = 0$. The results are presented for power law spectrum of kinetic energy with $\gamma = 1.5$ and 3.0. *Note* that in this case the distance is measured from the top point of the rock.

different zenith angles, η, is shown in Figure 10 along with the value for an exposure in free space for crystal orientations, $\beta = 0$ and $\pi/2$. In both cases the calculations are for a single exponent $\gamma = 3.0$ in the kinetic energy spectrum of the VH group of nuclei.

Finally, we show in Figure 11, the calculated track production rate for a spherical rock of radius 5 cm partially buried on the surface of a parent body. The calculations are for different amounts of burial. The results for two different spectral forms are shown for the crystal orientation, $\beta = 0$ as a function of depth measured along the vertical direction through the centre ($\eta = 0$).

The above illustrations clearly bring out the sharp contrast in the case of track production rate between exposure in space and on a parent body. We summarize below the salient features and contrasts in track production rates for the 2π and 4π irradiation geometries considered.

In the case of exposure on a parent body, the track production rate is highly dependent on the sample position as well as orientation defined by the angles η and δ, in contrast to an exposure in space where it is independent of these variables because of centro-symmetric irradiation geometry. As can be seen from the figures presented above, the asymmetric irradiation geometry in the case of an exposure on a parent body (e.g., Moon) does lead to an observable variation in the absolute track density values as well as in the track gradient along different radial directions. This fact must

be taken into account in interpreting track data from lunar samples. (As discussed later similar considerations hold in the case of 'isotope' production by low energy cosmic ray particles).

The results of the calculations presented in Figures 6–11 also clearly bring out the fact that β which is the angle between normal to the crystal plane and the radial direction through the detector does not uniquely define the sample orientation in the case of exposure on a parent body. The requirement of additional angle variables (δ, ζ, ξ) for defining the detector orientation is clear from Figures 3, 4 and 5. Thus except for the case when $\beta = 0$, a straightforward comparison between the results of calculation for space and parent body exposure is not meaningful. Therefore, for a fruitful comparison between 2π and 4π irradiation geometry we have, in most of the cases, considered here results for the case $\beta = 0$.

As can be seen from Figure 9, the track production rate at shallow depths for irradiation on a parent body is sensitively dependent on δ for values of η lying between 90° and 180°. However, for particular η values: $\eta = 0°$ and 180° and at the center of the rock for any values of η, the track production rate is independent of δ because of symmetry.

Also, it is evident from Figure 8 that the iso-track density profiles in the case of exposure on a parent body are not centrosymmetric as in the case of exposure in free space. As expected, the minimum track density point, c (see figure 8) is shifted downward from the center of the rock and lies at a distance ~ 1.6 times radius from the top of the rock. The position of the minimum corresponds to the point within the rock where the mean penetration distance, $\bar{r}$, is maximum: The value of $\bar{r}$ is given by:

$$\bar{r} = \frac{1}{2\pi} \int\limits_{0}^{2\pi} \int\limits_{0}^{\pi/2} r(\theta, \phi) \sin\theta \, d\theta \, \phi. \tag{12}$$

We show in Figure 12 the depth dependence of the parameter $\bar{r}$ on the zenith angle η, for a rock exposed on a parent body. A comparison of Figures 8 and 12 clearly shows that the shape of the iso-track contour is to a large extent governed by the variation in the average value of the penetration distance $\bar{r}$, and the exponent γ in the kinetic energy power-law spectrum primarily determines the shape of the track production spectrum within the rock.

We would like to point out an interesting feature in the track production profile for a partially buried rock exposed on a parent body (see Figures 5 and 11). This irradiation geometry is applicable to several of the lunar rocks. If a rock is buried by more than half the radius of the body, the track density decreases monotonically with depth along the $\eta = 0$ vertical direction. However, for cases when the depth of burial is smaller, the track density goes through a minimum (c.f. Figures 8 and 11). The reason for this is a purely geometrical one. The bottom portion of a non-buried rock receives relatively more flux of track producing nuclei than at points situated just above. Reference is made here to Figure 12 which brings out this point in terms of the shielding parameter $\bar{r}$, the mean penetration distance.
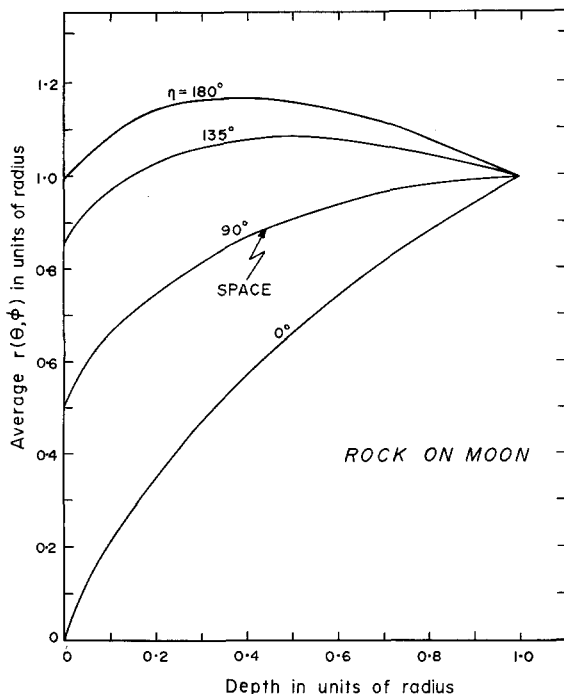
Fig. 12. Average value of $r(\theta, \phi)$ as a function of depth is plotted in unit of radius for various zenith angles η.

TABLE I

Values of best fit parameters K and α in the track production profile $\varrho(X) = KX^{-\alpha}$, for different primary kinetic energy spectra of VH group nuclei expressed as $dN = \text{const.}\ E^{-\gamma}\ dE$. The integrated flux $N\ (\geqslant 3\ \text{BeV})$ is taken to be 1 particle $\text{cm}^{-2}\ \text{s}^{-1}$ sr^{-1}. The calculations are for a large-sized object $(R \sim 100\ \text{cm})$ of lunar composition

Parameters related	Depth interval	
	0.001–0.1 cm	0.10–5.0 cm
α, γ	$\alpha = 1.2\gamma^{0.72}$	$\alpha = 1.2\gamma^{0.61}$
K, γ	$K = 4.0 \times 10^9\gamma^{6.3}$	$1.7 \times 10^9\gamma^{7.3}$

Finally, we give here convenient empirical relationships between calculated track production rates and depth for the case of a large-sized object. The best fit parameters for a power law track production profile are shown in Table I as a function of the exponent of the kinetic energy power-law spectrum. The range of γ value chosen is between 1 and 5 which adequately covers the values observed for both low energy and high energy cosmic rays.

3. Rate of Production of Low Threshold Radionuclides by Solar Cosmic Rays in Centimeter-size Objects: 4π and 2π Irradiation Geometries

It is now well known that cosmic ray bombardment in space results in the production of a host of radionuclides. It is found convenient (cf. Lal, 1972; Reedy and Arnold, 1972) to discuss this production separately as due to interactions of (i) low energy particles primarily of solar origin and (ii) high energy particles (and their secondaries) of galactic origin. In this paper, we will primarily concern ourselves with the first agency of isotope production, viz. nuclear interactions of low energy cosmic rays sporadically accelerated by sun during solar flares. As was mentioned earlier, this problem could not easily be studied with meteorites because of ablation (cf. Amin *et al.*, 1969). However, the results of analyses of lunar samples clearly show that it is possible to see the effects of one or two recent flares (via analysis of short lived nuclides, Co^{56}, Na^{22}) as well as the long term averaged solar particle irradiation effect by studying long lived nuclides Al^{26}, Mn^{53} etc. Hence, it has become important to evaluate theoretically the production profiles for low threshold isotopes due to solar flare radiation.

3.1. GENERAL ANALYTICAL EXPRESSION FOR THE RATE OF PRODUCTION OF RADIONUCLIDES

In general the isotope production rate $Q(X)$, of a radionuclide at depth X within an object is given by

$$Q(X) = \sum_j \frac{NK_j}{A} \int\limits_E \int\limits_\phi \int\limits_\theta \sum_i g_i(X, E, \theta, \phi)\, \sigma_{ij}(E) \sin\theta\, d\theta\, d\phi\, dE, \qquad (13)$$

where

N is the Avogadro's number;

k_j is the fractional abundance by weight of a particular target nuclide, j, in the object;

$g_i(X, E, \theta, \phi)$ is the differential kinetic energy spectra of the nuclear interacting component, i, of cosmic radiation, both primary and secondary;

θ, ϕ are the zenith and azimuthal angles respectively and $\sigma_{ij}(E)$ is the cross-section for the production of a nuclide of interest in collision of the particle of component i with target nuclide j at kinetic energy E.

The excitation functions are fairly well known for radionuclides of interest. The principal uncertainty at present lies in the estimation of $g_i(X, E, \theta, \phi)$ for the case of galactic cosmic rays (cf. Kohman and Bender, 1967; Amin *et al.*, 1969; Venkata-varadan, 1970; Reedy and Arnold, 1972). The problem is however, rather straightforward for the case of solar rays because the time-averaged kinetic energy spectrum in a flare event is usually very soft so that the nucleonic cascade effects are usually not important. Furthermore, the solar cosmic ray flux has been experimentally found to be sufficiently large so that isotope production in the top centimeters amounts to a value which is 20–50% or larger compared to the contribution due to galactic cosmic rays (Shedlovsky *et al.*, 1970; Finkel *et al.*, 1971; Wahlen *et al.*, 1972). In view of this

and since the function $g_i(\theta, \phi)$ is not very depth sensitive for galactic cosmic rays (Lavrukhina *et al.*, 1969; Kohman and Bender, 1967) it is experimentally possible to separate out the solar cosmic ray effects fairly accurately. In the following, we will, therefore, consider theoretically the isotope production rates for shallow depths for objects of different sizes exposed in free space or on a parent body.

At different times within a flare event, or averaged over one flare or several flares, the solar particle spectra can be very well represented (Biswas and Fichtel, 1965; Lal
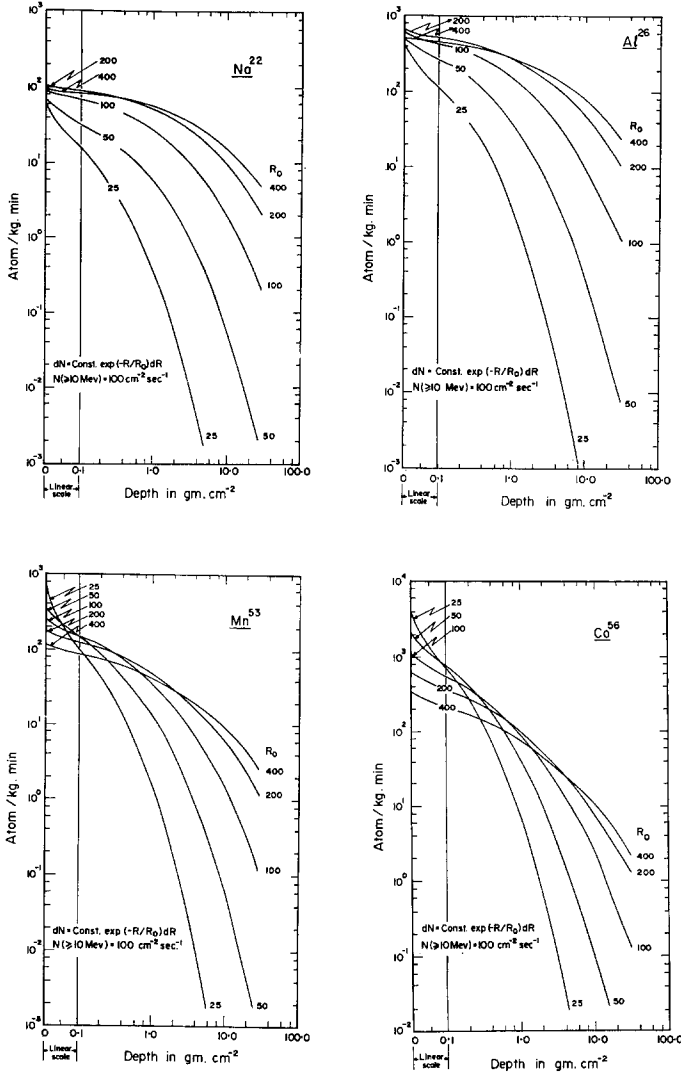

Fig. 13. Calculated production rates of radio isotopes Na^{22}, Al^{26}, Mn^{53}, and Co^{56} in Moon due to solar protons. The kinetic energy spectrum of protons is assumed to be an exponential rigidity type. Calculations refer to $R_0 = 25$, 50, 100, 200 and 400 MV with omni-directional proton flux above 10 MeV $= 100$ cm^{-2} s^{-1} in all cases.

and Venkatavaradan, 1967) by an exponential rigidity spectra of the type

$$dN = \text{const. } \exp\left(-R/R_0\right) dR,\tag{14}$$

where R is the rigidity and R_0 is the characteristic rigidity, the value of which usually lies between 25–400 MV at different times within an event.

The analytical expressions for $g(X, R)$ and $g(X, E)$ for rigidity type spectrum (Equation (14)) and the kinetic energy power law spectrum (Equation (11)), corresponding to traversal of distance X, have been discussed by Lal (1972). The resulting kinetic energy spectra of solar protons or alpha particles at any point in the rock $g(X, E, \theta, \phi)$ can then be deduced by using analytical functions for penetration depths $r(\theta, \phi)$ discussed in Section 2.

Below we present results of some calculations of isotope production rates in case of the low threshold nuclides Na^{22}, Al^{26}, Mn^{53}, Co^{56} and Ni^{59}.

3.2. RESULTS OF CALCULATION OF PRODUCTION RATES OF RADIONUCLIDES FOR 4π AND 2π IRRADIATION GEOMETRY

The results of calculation of isotope production rates are presented in Figures 13 to 18 for objects irradiated in free space and also for irradiation on a parent body. Expo-
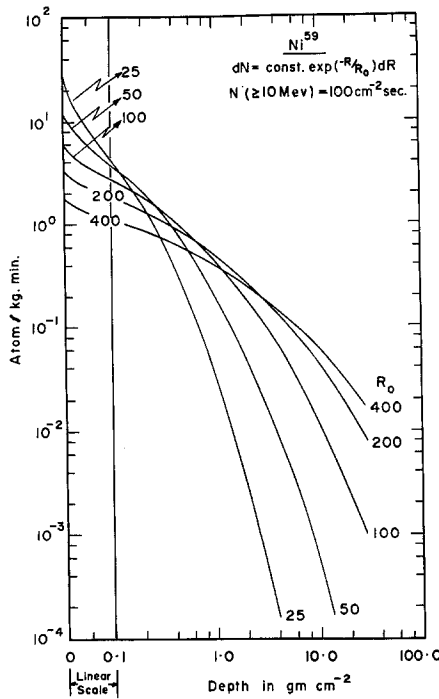

Fig. 14.   Calculated production rates of Ni^{59} in Moon due to solar protons and alpha particles. The kinetic energy spectrum of protons is assumed to be an exponential rigidity type. Calculations refer to $R_0 = 25$, 50, 100, 200 and 400 MV with omni-directional proton flux above 10 MeV = 100 cm^{-2} s^{-1}. The p/α ratio in the cosmic ray beam is taken to be 11.
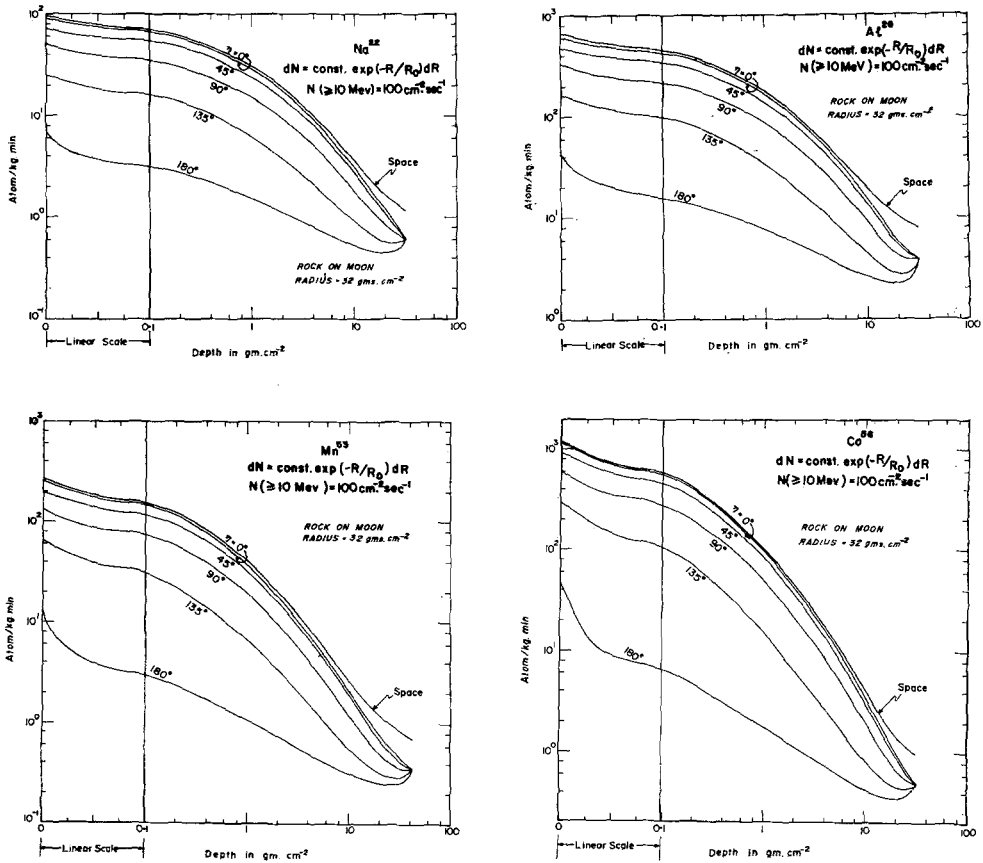
Fig. 15. Calculated production rates of Na[22], Al[26], Mn[53] and Co[56] as a function of depth X for various values of zenith angle η in 2π exposure on moon for a spherical rock of radius 32 gm cm^{-2}. The kinetic energy spectrum of protons is assumed to be an exponential rigidity type. Calculations refer to $R_0 = 100$ MV with omni-directional proton flux above 10 MeV $= 100$ cm^{-2} s^{-1}.

nential rigidity spectral form (Equation (14)) has been assumed to hold. The calculations are presented for $R_0 = 25, 50, 100, 200$ and 400 MV. The constant in Equation (14) corresponds to an omni-directional flux of 100 protons cm^{-2} s^{-1} for protons of kinetic energy exceeding 10 MeV. Excitation functions are based on published values (see Venkatavaradan, 1970; Lal, 1972; Reedy and Arnold, 1972, and Tanaka et al., 1972). In Figure 13 we show the depth-dependence in the production rates of the radionuclides Na[22], Al[26], Mn[53] and Co[56] in moon for R_0 values lying between 25 to 400 MV. Similar calculations are shown for the production of Ni[59] due to solar proton and alpha particles in Figure 14, assuming integrated proton to alpha-particles ratio to 11 (Biswas and Fichtel, 1965).

Production profiles for the five radio-nuclides are shown in Figures 15 and 16 for a body of radius 32 gms cm^{-2} of lunar composition, exposed on a parent body for
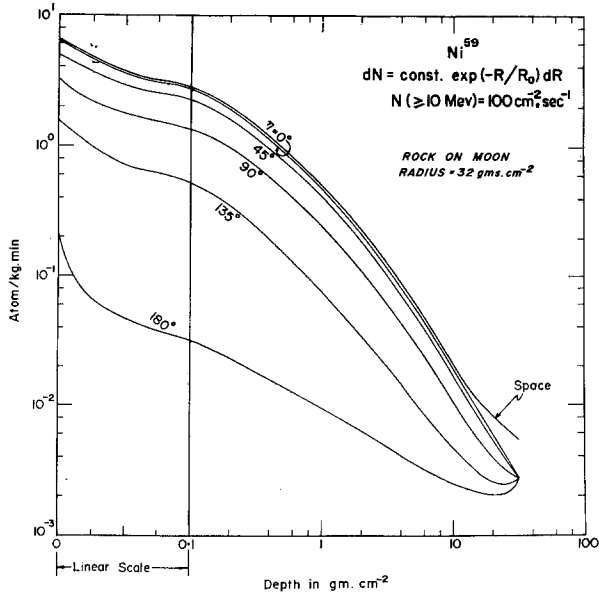
Fig. 16. Calculated production rates of Ni[59] as a function of depth for various values of zenith angle η in 2π exposure on Moon for a spherical rock of radius 32 gm cm^{-2}. The kinetic energy spectrum of protons is assumed to be an exponential rigidity type. Calculations refer to $R_0 = 100$ MV with omni-directional proton flux above 10 MeV $= 100$ cm^{-2} s^{-1}. The p/α ratio in the cosmic ray beam is taken to be 11.
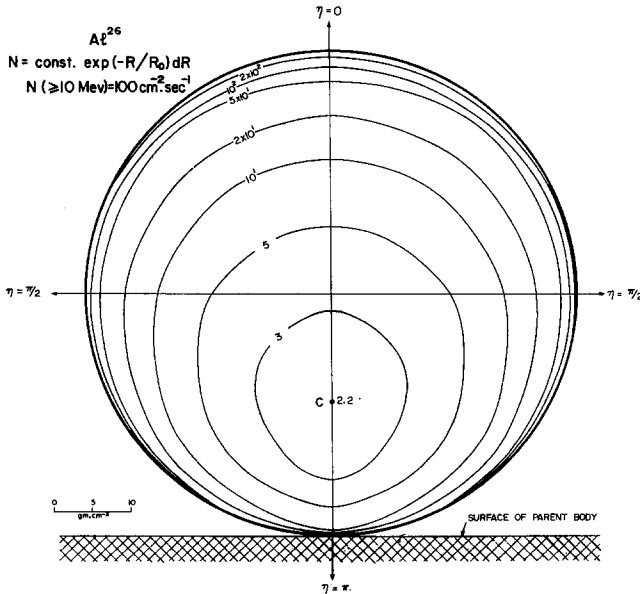

Fig. 17. Iso-production contours for Al[26] in a vertical section through the center for 2π exposure of a rock of radius 32 gm cm^{-2} on lunar surface. The kinetic energy spectrum for protons is assumed to be an exponential rigidity type. Calculations refer to $R_0 = 100$ MV with omni-directional proton flux above 10 MeV $= 100$ cm^{-2} s^{-1}.
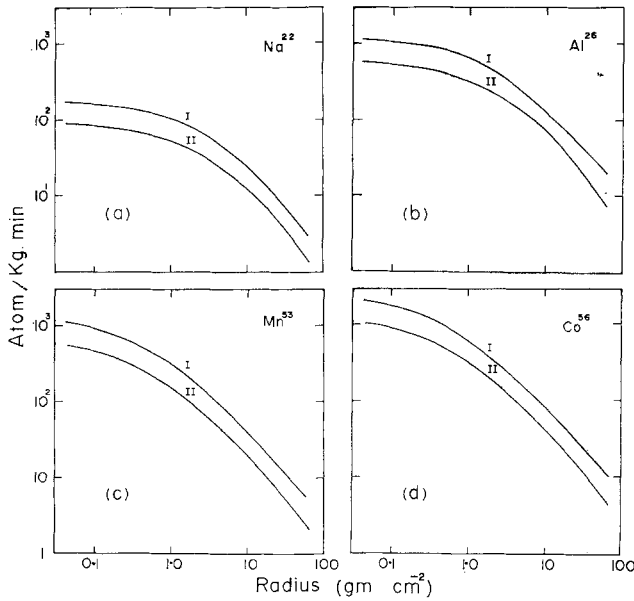
Fig. 18. The production rate in atom kg^{-1} min^{-1} averaged over the *whole rock* is plotted as a function of the radius of the rock for four low-threshold isotopes Na^{22}, Al^{26}, Mn^{53} and Co^{56}. I and II refer to 2π and 4π irradiation geometries, respectively. Note that over a wide range of radius, 3 to 64 gm, cm^{-2}, the whole-rock-averaged production rate is approximately inversely proportional to the radius. Proton spectrum is assumed to be an exponential rigidity type with $R_0 = 100$ MV.

$R_0 = 100$ MV and different radial directions η. In each case, for comparison, we have also shown the calculated production rates for exposure in free space. Based on the above data we have shown in Figure 17 the iso-production contours for radionuclide Al^{26} for the case of exposure of a rock of radius 32 gm cm^{-2} on a parent body for $R_0 = 100$ MV. We show in Figure 18 the average production rate in atom kg^{-1} min^{-1} for the *whole rock*, as a function of radius of the rock (between 0.1 gm cm^{-2} to 60 gm cm^{-2}).

Finally, we present in Table II, best fit parameter β in the power law isotope production expressed as $KX^{-\beta}$.

As discussed earlier in the case of fossil tracks (see Section 2) the production of radionuclides depends on the geometry of irradiation to a large extent. As can be seen from Figures 15 and 16, the production rates along different radial directions for an exposure on a parent body differ by almost an order of magnitude. The asymmetric isotope production along $\eta = 0$ direction with respect to the center of the rock (see Figure 17) again, analogous to the case of tracks, is primiarily a manifestation of an asymmetry in the 'shielding' parameter (see Figure 12). Consequently, the minimum isotope production point, C, is shifted downwards from the center for the case of 2π irradiation.

Another interesting feature of the low energy solar particle phenomena can be seen

TABLE II

Values of best fit parameter β in the production profiles, $Q(X) = \text{const. } X^{-\beta}$, of cosmogenic radioisotopes Na^{22}, Al^{26}, Mn^{53}, Co^{56} and Ni^{59}. The primary proton spectrum is assumed to be $dN = \text{const. } \exp(-R/R_0)\,dR$ with omnidirectional flux $N\ (\geqslant 10 \text{ MeV}) = 100 \text{ cm}^{-2} \text{ s}^{-1}$. Calculations are for a large size object (Radius $= 100 \text{ gm cm}^{-2}$) of lunar composition. The parameters β and R_0 are related by empirical relations listed in the table for two depth intervals. ϱ is the density of the material (gm cm^{-3}).

Isotope	Depth interval (gm cm^{-2})	
	$0 \leqslant x \leqslant 0.1\,\varrho$	$0.1\,\varrho \leqslant x \leqslant 1.0\,\varrho$
Na^{22}	$\beta = 26.0\ R_0^{-1.03}$	$\beta = 44.0\ R_0^{-0.83}$
Al^{26}	$\beta = 14.0\ R_0^{-0.86}$	$\beta = 35.0\ R_0^{-0.82}$
Mn^{53}	$\beta = 11.6\ R_0^{-0.75}$	$\beta = 30.0\ R_0^{-0.74}$
Co^{56}	$\beta = 6.8\ R_0^{-0.57}$	$\beta = 24.0\ R_0^{-0.65}$
Ni^{59}	$\beta = 8.7\ R_0^{-0.61}$	$\beta = 25.5\ R_0^{-0.67}$

from Figure 18. Because of the steep depth dependence in isotope production rate at larger depths, the average production rate in atom $\text{kg}^{-1} \text{min}^{-1}$ for the whole rock varies inversely as its radius except for very small values of radius < 3.0 mm, a region where isotope production is not very depth sensitive (Figure 15).

Thus, clearly observable differences exist for production of isotopes of interest due to solar particles for the case of irradiation in space and on a parent body.

4. Summary

We have presented illustratory calculations of the absolute magnitude of low energy cosmic ray induced effects in extraterrestrial objects, confining to production of 'etchable tracks' and 'isotopes'. The production profiles cease to be centrosymmetric in all the three dimensions for the case of irradiation on a parent body. The parameters required to define the orientation of the sample studied are discussed and the dependence of magnitude of the cosmogenic effect is investigated in detail; results are presented graphically and also in convenient analytical forms in some cases.

Present work clearly brings out the contrast in low-energy cosmogenic effects for bodies exposed in space or on a parent body. These results are not merely of academic importance because of the availability of a large number of lunar rocks having diverse and complex irradiation histories. The interpretation of cosmogenic data is shown to be very sensitively dependent on the irradiation geometry. In practice, further complications in patterns of cosmogenic effects arise due to multiple exposure history, fragmentation and erosion during irradiation. For delineating cosmic ray history, it thus becomes necessary to work with rocks having the simplest exposure history, and present calculations should prove very useful in this connection.

Acknowledgements

Appendix I. Best Fit Parameters for the Range Energy Polynomial for Fe^{56}, Kr^{84} and Xe^{132} Ions in Moon and Meteorites

Ion ranges for $0.01-10^4$ MeV n^{-1} kinetic energy for three ions of interest in fossil track work Fe^{56}, Kr^{84} and Xe^{132} were calculated in materials of lunar and meteoritic composition using the computer program 'RANGENER' of Henke and Benton (1967). To the calculated set of range and energy values a five degree polynomial of the following form is fitted:

$$\ln E = a_0 + a_1 \ln(KS) + a_2 [\ln(KS)]^2 + a_3 [\ln(KS)]^3 +$$
$$+ a_4 [\ln(KS)]^4 + a_5 [\ln(KS)]^5 \qquad (I.1)$$
$$(K = \varrho_a/\varrho_M)$$

where ϱ_a is an adopted value of the density (gm cm^{-3}) for the target material and ϱ_m is the actual density of the target material of identical composition; S is the range (cm) of the ion. E is the kinetic energy per nucleon expressed as BeV n^{-1}.

In fitting the above polynomial, the range S has been taken as the independent variable and the energy E as the dependent variable. The reason for this is that in

TABLE I.1

Adopted values of chemical compositions and densities of lunar and meteoritic materials

Material	Chemical composition (weight percent)	Density, ϱ_a (gm cm^{-3})
Moon (Average of Apollo 11 through 16)	Mn = 0.26, Na = 0.37, Cr = 0.40 Ti = 3.92, Mg = 6.00, Al = 6.00, Ca = 7.40, Fe = 15.45; Si = 18.75, O = 40.90, Others = 0.55	3.40
Chondrite (Average of H & L Group)	Ti = 0.11, Mn = 0.26, Cr = 0.35, Na = 0.68, Al = 1.30, Ni = 1.25, Ca = 1.40, S = 2.25, Mg = 14.00, Si = 18.00, Fe = 25.00, O = 35.00 Others = 0.30	3.58
Mesosiderite	P = 0.11, Na = 0.13, Mn = 0.17, Cr = 0.24, Co = 0.28, S = 1.00, Ca = 2.07, Al = 2.17, Mg = 3.83, Ni = 4.71, Si = 9.26, O = 18.30, Fe = 53.57, Others = 4.08	4.58

TABLE I.2

Best fit values of the range–energy polynomial coefficients for low energy (0.01–10^2 MeV n^{-1}) region

Projectile	Target medium	Coefficients					
		a_0	a_1	a_2	a_3	a_4	a_5
$_{26}$Fe^{56}	Moon (Average Apollo 11–16)	−1.33998	0.74272	0.04310	−0.00268	−0.00219	−0.00012
	Chondrite (Average H & L Group)	−1.30052	0.75436	0.04661	−0.00218	−0.00214	−0.00012
	Mesosiderite	−1.09310	0.87382	0.09528	0.00743	−0.00122	−0.00009
$_{36}$Kr^{84}	Moon (Average Apollo 11–16)	−1.03316	0.96239	0.13864	0.01597	−0.00086	−0.00009
	Chondrite (Average H & L Group)	−0.98328	0.98324	0.14502	0.01682	−0.00078	−0.00009
	Mesosiderite	−0.73337	1.14055	0.20646	0.02852	0.00031	−0.00005
$_{54}$Xe^{182}	Moon (Average Apollo 11–16)	−0.57839	1.26311	0.26390	0.04051	0.00090	−0.00006
	Chondrite (Average H & L Group)	−0.51908	1.29055	0.27174	0.04139	0.00096	−0.00006
	Mesosiderite	−0.26447	1.43954	0.32648	0.05145	0.00191	−0.00002

TABLE I.3

Best fit values of range-energy polynomial coefficients for high energy (80–10^4 MeV n^{-1}) region

Projectile ion	Target medium	Polynomial coefficients					
		a_0	a_1	a_2	a_3	a_4	a_5
$_{26}Fe^{56}$	Moon (Average Apollo 11–16)	−1.46993	0.61018	0.00956	0.00031	0.00030	0.00020
	Chondrite (Average H & L Group)	−1.44161	0.61130	0.00958	0.00037	0.00035	0.00020
	Mesosiderite	−1.33170	0.61750	0.00953	0.00069	0.00053	0.00021
$_{36}Kr^{84}$	Moon (Average Apollo 11–16)	−1.32612	0.62013	0.00889	0.00085	0.00045	0.00021
	Chondrite (Average H & L Group)	−1.29734	0.62123	0.00898	0.00094	0.00050	0.00021
	Mesosiderite	−1.18558	0.62760	0.00915	0.00139	0.00070	0.00023
$_{54}Xe^{132}$	Moon (Average Apollo 11–16)	−1.11400	0.63515	0.00902	0.00185	0.00066	0.00025
	Chondrite (Average H & L Group)	−1.08453	0.63631	0.00923	0.00198	0.00072	0.00025
	Mesosiderite	−0.97004	0.64335	0.00990	0.00263	0.00096	0.00027

calculating the track production rate at a given point inside a body one has first to calculate the penetration distance of flight, $r(\theta, \phi)$, of a cosmic ray particle inside the target material and then deduce the corresponding kinetic energy of the particle. Fit is made for $\ln E$ vs. $\ln S$ because over a wide range of values in E and S, $S \propto E^{\text{const}}$.

In Table I.1, we give the adopted values of the denisties, ϱ_a, and the chemical compositions for the lunar samples and meteorites. In Table I.2 and I.3 are tabulated the best fit values of the polynomial coefficients for Fe^{56}, Kr^{84} and Xe^{132} for lunar and meteoritic target materials, separately for the low energy (0.01 to 10^2 MeV n^{-1}) and the high energy (80–10^4 MeV n^{-1}) intervals.

Appendix II. Interaction Mean Free Path and Fragmentation Factors

We are interested in the total interaction probability, λ, and the fragmentation factor $F(Z \to Z')$, for multicharged nuclei in relevant target materials of different compositions. Direct experimental information is not available but reasonable values can be estimated for these parameters, based on studies of nuclear interactions of heavy nuclei in nuclear emulsions and general spallation systematics for proton induced reactions in medium and heavyweight target nuclei (Rudstam, 1956; Durgaprasad, 1964: Waddington, 1960; Shapiro and Silberberg 1970).

Below we discuss the values adopted for the parameter λ and $F(Z \to Z')$ for different multicharged ions of interest in track work.

II. 1. TOTAL NUCLEAR INTERACTION PROBABILITY FOR MULTICHARGED IONS

We adopt the semi-empirical relation proposed by Durgaprasad (1964) for the nuclear interaction cross-section, σ_i, for an ion of mass number A_i in a target of mass number A_t.

$$\sigma_i = \pi r_0^2 \left(A_i^{1/3} + A_t^{1/3} \right), \tag{II.1}$$

The average cross-section per atom for materials of lunar and meteoritic composition is calculated on the basis of Equation (II. 1) for chemical composition as given in Table I. 1.

TABLE II.1

Ion	Interaction mean free path L in cm		
	Moon rock	Chondrite	Mesosiderite
$_{18}Ar^{36}$	7.14	6.99	6.85
$_{26}Fe^{56}$	6.06	5.94	5.87
$_{36}Kr^{84}$	5.17	5.06	5.04
$_{54}Xe^{132}$	4.28	4.20	4.21

The corresponding value of the average mean free path, L, in the target material, which is inverse of the interaction probability, λ, is related to the average cross-section, σ, through the relation

$$\lambda\,(\mathrm{cm}^{-1}) = 1/L = N\sigma. \tag{II.2}$$

The calculated values of L for different targets are summarized in Table II. 1 for ions Ar^{36}, Fe^{56}, Kr^{84} and Xe^{132} as illustration.

II. 2. THE FRAGMENTATION FACTOR, $F(Z \to Z')$ FOR MULTICHARGED IONS IN TYPICAL SILICATE MATERIALS

The calculation of track formation rates involves a knowledge of the number and energy of both the *primary* and *secondary* track forming nuclei as a function of depth in the object. The latter requires a knowledge of the yield per nuclear interaction of nuclei of atomic number exceeding a certain minimum value, Z' which can form etchable tracks. It can be easily shown that the number of nuclei of atomic number lying between Z and Z', after a traversal of a distance X, is given by

$$N = N_0 e^{-\lambda X}\, F(Z \to Z'), \tag{II.3}$$

where N_0 is the initial number of nuclei of atomic number Z, and $F(Z \to Z')$ defined as the fragmentation factor given by

$$F(Z \to Z') = 1 + \lambda X F_0 + (1/2!)\,(\lambda X)^2\, F_0 F_1 + \cdots. \tag{II.4}$$

In Equation (II.4), F_0, F_1, $F_2 \ldots$ etc. are the fragmentation parameters of various orders and represent the fractional yields of secondary nuclei within the group $(Z - Z')$ in successive nuclear interactions of primary nuclei and second and higher generation secondaries.

Iron group nuclei are the most abundant of the track forming nuclei in common silicate minerals. Moreover, track production rate is proportional to the recordable range ΔR, of the track forming nuclei (see Equation (1) in text), and since the recordable range decreases rapidly with decreasing atomic number, one can safely neglect the higher order fragmentation parameters, F_1, $F_2 \ldots$ in Equation (II.4), for the purposes of our calculations.

In Equations (II.3) and (II.4), implied is the assumption that the total nuclear interaction probability λ and fragmentation parameters e.g. F_0 are energy independent. This is not true, particularly for the fragmentation parameter F_0, which is proportional to the partial cross-section for the formation of secondary nuclei $(Z - Z')$ in a given nuclear interaction. Below we present a model calculation for deducing the effective energy important in estimating the fragmentation parameter, F_0.

Let σ be the partial cross-section for the formation of a secondary of atomic number Z_i in nuclear interaction of particles of atomic number Z in the target. In general σ is energy dependent, particularly at low energies ($\leqslant 1$ BeV n^{-1}), an energy region of

interest in the fossil track work. The mean effective cross-section $\bar{\sigma}(X)$ will depend both on the excitation function $\sigma(E)$ as well as the depth of observation, X. Although, at a given point of observation in a rock, particles arrive from different directions having different penetration distances, for simplicity, we will consider here the case of a straight line traversal of particles. The effective cross-section, as a function of penetration distance, X, at the point of observation, is then given by

$$\bar{\sigma}(X) = \frac{\displaystyle\int_0^X e^{-\lambda y}\, \sigma(E(y))\, \mathrm{d}y}{\displaystyle\int_0^X e^{-\lambda y}\, \mathrm{d}y}, \tag{II.5}$$

where $\sigma(E(y))$ is the value of the partial cross-section for formation of secondary of atomic number, Z_i at the kinetic energy, $E(y)$, which a primary particle of total range X will have after travelling a distance y. The corresponding value of the effective energy, E_{eff}, as a function X can then be obtained from the excitation function $\sigma(E)$.

For a wide range of excitation functions, as shown in Fig. II.a, we have calculated the effective values for the cross-section, $\bar{\sigma}(x)$, and energy as a function of depth, inside a body of radius 25 cm. The results are shown in Figures IIb and IIc, respectively. As can be seen from Figure IIc, the value of E_{eff} lies in the range of few hundred MeV's for observation point at depths greater than few cm. (At smaller depths, the fragmentation contributions are in any case not important since the interaction mean free path, $L = 1/\lambda$, is of the order of 5–6 cm in different target materials of interest; see Table II.1). This is so because of the fact that an incident particle traverses most of its total range at an energy close to its initial value, i.e. the energy at $X = 0$, due to the power law form of the 'Range-Energy' relation.
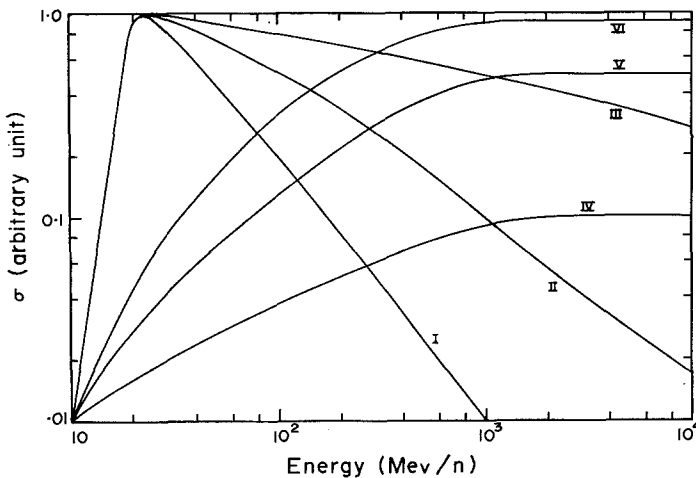

Fig. IIa.   Assumed shape of the excitation function used in calculation of fragmentation parameter F_0.
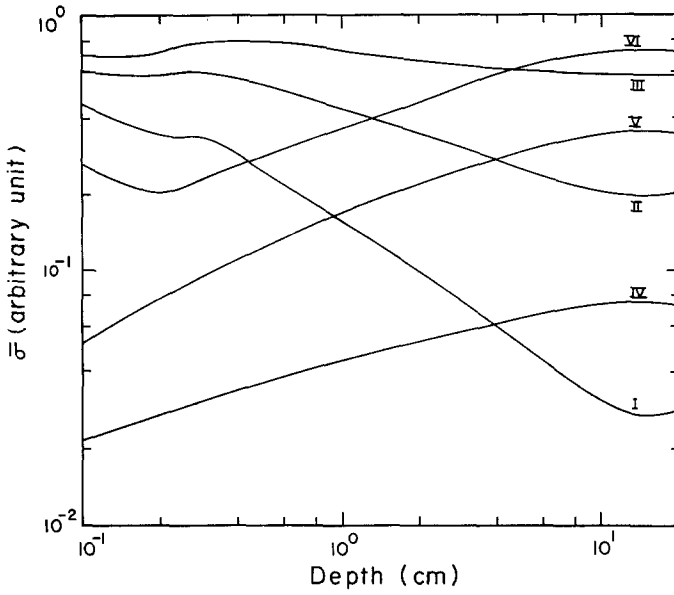
Fig. IIb.   The effective cross-section $\bar{\sigma}$ is plotted as a function of depth of the point of observation of tracks for different assumed excitation functions given in Figure IIa.
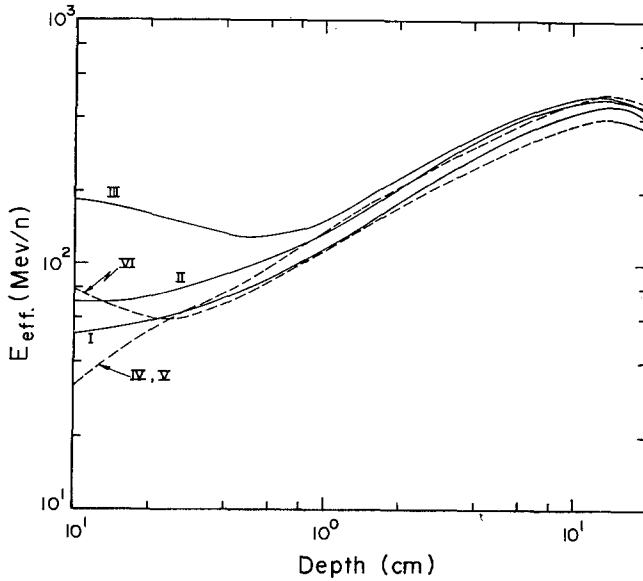

Fig. IIc.   The effective energy E_{eff} is plotted as a function of depth of the point of observation of tracks, based on curves in Figure IIa and IIb.
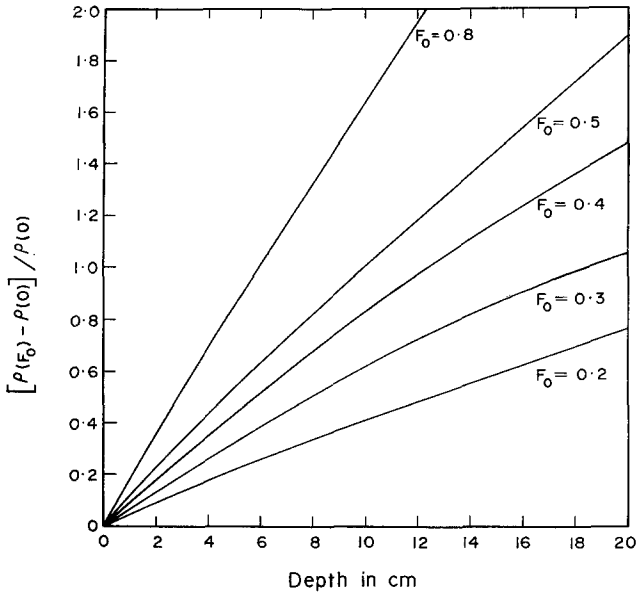
Fig. IId. The quantity plotted along the ordinate represents the fractional increase of tracks contributed by multicharged secondary nuclei produced in collisions. Higher values of F_0 correspond to a larger production cross-section for track forming nuclei.

The above model calculations clearly show that experimental data in the range of 200–500 MeV n^{-1} are necessary for estimating the fragmentation factor, $F(Z \to Z')$ due to interactions of multicharged nuclei in medium weight target nuclei. Although no cross-section data are as yet available, one can make some approximate guesses based on the data for proton induced reaction in medium and heavyweight target nuclei. Based on the literature values (cf. Tamhane, 1972) we can set an upper limit of 0.2 for F_0 and this is the value adopted in calculations presented here. In order to study the errors due to an uncertainty in the fragmentation parameter, F_0, on the track production rate, we have plotted in Figure IId, contribution to track formation due to secondaries, for different values of F_0. As can be seen from this figure, this contribution is less than 20% for depths less than 5 cm in the case of $F_0 = 0.2$. Thus any uncertainty in the fragmentation factor F_0 will become important only for depths greater than ~ 10 cm.

Appendix III. Calculation of Radial Distance $r(\theta, \phi)$ from any Given Point Within an Ellipsoid of Semi-Axes a, b and c

The distance travelled by a cosmic ray particle between pt. A and the surface along (θ, ϕ) direction with origin at A (Figure 4) is $QA = r(\theta, \phi)$, which satisfies the relation

$$\frac{1}{a^2} \left[r(\theta, \phi) \sin\theta \cos\phi + OA \sin\eta \cos\zeta \right]^2 +$$

$$+ \frac{1}{b^2} \left[r(\theta, \phi) \sin\theta \sin\phi + OA \sin\eta \sin\zeta \right]^2 +$$

$$+ \frac{1}{c^2} \left[r(\theta, \phi) \cos\theta + OA \cos\eta \right]^2 = 1, \qquad (III.1)$$

where the co-ordinates of the point A are fixed by the distance OA, the zenith angle η and the azimuth angle ζ (w. r. t. pt. O). If $X(=SA)$ denotes the depth of the point of observation A from the nearest surface, then $OA = OS - SA$. Value of $OS = r_0$ is given by

$$r_0^2 = OS^2 = \frac{a^2 b^2 c^2}{a^2 b^2 \cos^2\eta + b^2 c^2 \cos^2\zeta \sin^2\eta + c^2 a^2 \sin^2\eta \sin^2\zeta}. \qquad (III.2)$$

The solution for $r(\theta, \phi)$ from Equations (III.1) and (III.2) can be written explicitly as

$$r(\theta, \phi) = \frac{1}{U} \left[-V + [V^2 - U(W-1)]^{1/2} \right], \qquad (III.3)$$

where

$$U = \frac{\sin^2\theta \cos^2\phi}{a^2} + \frac{\sin^2\theta \sin^2\phi}{b^2} + \frac{\cos^2\theta}{c^2}, \qquad (III.4)$$

$$V = (r_0 - X) \left[\frac{\sin\theta \sin\eta \cos\phi \cos\zeta}{a^2} + \right.$$

$$\left. + \frac{\sin\theta \sin\phi \sin\eta \sin\zeta}{b^2} + \frac{\cos\theta \cos\eta}{c^2} \right], \qquad (III.5)$$

and

$$W = (r_0 - X)^2 \left[\frac{\sin^2\eta \cos^2\zeta}{a^2} + \frac{\sin^2\eta \sin^2\zeta}{b^2} + \frac{\cos^2\eta}{c^2} \right]. \qquad (III.6)$$

Special case: $a = b = c = R$

In this case, $r_0 = R$ and the ellipsoid degenerates into a sphere. Here ζ can be taken as π without any loss of generality. From (III.4), (III.5) and (III.6)

$$U = \frac{1}{R^2}, \qquad (III.7)$$

$$V = \frac{(R-X)}{R^2} \left[\cos\theta \cos\eta - \sin\theta \sin\eta \cos\phi \right], \qquad (III.8)$$

$$W = \frac{(R-X)^2}{R^2}, \qquad (III.9)$$

and we obtain for $r(\theta, \phi)$ the expression

$$r(\theta, \phi) = (\sin\theta \sin\eta \cos\phi - \cos\theta \cos\eta)(R - X) +$$
$$+ [(R - X)^2 \{(\cos\theta \cos\eta - \sin\theta \sin\eta \cos\phi)^2 - 1\} + R^2]^{1/2}.$$
$$\text{(III.10)}$$

We note here that the expression $(\cos\theta \cos\eta - \sin\theta \sin\eta \cos\phi) = \cos\gamma$ where γ is the angle $\angle QAO$; cf. expression 9 in main text. Therefore,

$$r(\theta, \phi) = -(R - X)\cos\gamma + [R^2 \cos^2\gamma + 2RX \sin^2\gamma - X^2 \sin^2\gamma]^{1/2},$$
$$\text{(III.11)}$$

which is the same as Equation (8) in the main text for the spherical case.

Appendix IV. Analytical Expressions for Track Registration Inside a Partially Buried Ellipsoidal Rock, on a Parent Body

The rate of track production due to nuclei of atomic number Z, $(\dot{\varrho})_{Z, X}$ at a point A (see Figure 5) is given by the sum of two integrals corresponding to different integration limits for θ:

(i) $0 \leqslant \theta \leqslant \theta_c(\phi)$, for the region corresponding to cosmic ray nuclei traversing the unburied cap of the rock;

(ii) $\theta_c(\phi) \leqslant \theta \leqslant \pi/2$, corresponding to nuclei traversing in the regolith and the buried portion of the rock. Thus

$$(\dot{\varrho})_{Z, X} = \int_{\phi=0}^{2\pi} \int_{\theta=0}^{\theta_c} \left[\frac{dN}{dE} \frac{dE}{dS}\right]_{r(\theta, \phi)} \Delta R(Z) \exp(-\lambda r(\theta, \phi)) \times$$
$$\times F(Z \to Z', r(\theta, \phi)) |\cos\alpha| \sin\theta \, d\theta \, d\phi +$$
$$+ \int_{\phi=0}^{2\pi} \int_{\theta=\theta_c}^{\pi/2} \left[\frac{dN}{dE} \frac{dE}{dS}\right]_{r(\theta, \phi)} \Delta R(Z) \exp(-\lambda r(\theta, \phi)) \times$$
$$\times F(Z \to Z', r(\theta, \phi)) |\cos\alpha| \sin\theta \, d\theta \, d\phi. \qquad \text{(IV.1)}$$

For the interval $0 \leqslant \theta \leqslant \theta_c(\phi)$, $r(\theta, \phi)$ is given by Equation (III.3) derived in Appendix III.

For $\theta \geqslant \theta_c(\phi)$ one notes that since the density of the regolith material may be markedly different from that of the rock, $r(\theta, \phi)$ should be expressed as the sum of two terms: one corresponding to the traverse in the rock and the other corresponding to the traverse in the regolith. Thus, while evaluating the second integral in Equation (IV.1), one has to use the density-normalised value $[r(\theta, \phi)]_{\text{norm}}$ of $r(\theta, \phi)$. If k is the ratio of the density of the regolith material to that of the rock, $[r(\theta, \phi)]_{\text{norm}}$ is given by (see Figure 9)

$$[r(\theta, \phi)]_{\text{norm}} = r(\theta, \phi)_{\text{rock}} + k r(\theta, \phi)_{\text{regolith}} \qquad \text{(IV.2)}$$
$$= (1 - k) r(\theta, \phi)_{\text{rock}} + k AA' \sec\theta, \qquad \text{(IV.3)}$$

since

$$r(\theta, \phi)_{\text{regolith}} = AA' \sec\theta - r(\theta, \phi)_{\text{rock}}.$$ (IV.4)

The expression for $r(\theta, \phi)_{\text{rock}}$ remains the same as in Equation (III.3) in Appendix III. The value of $r(\theta, \phi)_{\text{regolith}}$ given by Equation (IV.4) above involves AA', the depth of the point of observation from the level of the surface of the regolith and is given by

$$AA' = (B_d - c) - OA\cos\eta,$$ (IV.5)

B_b = the depth of burial of the rock (see Figure 9).

OA = distance of the point of observation from the center of the rock.

$= OS - SA = OS - X$. OS is given by Equation (III.2) in Appendix III.

The angle θ_c is a function of ϕ and is readily seen to be

$$\theta_c = \frac{\pi}{2} - \tan^{-1}[AA'/AT];$$ (IV.6)

AT is given by

$$AT = \frac{-L + (L^2 - MN)^{1/2}}{M},$$ (IV.7)

where

$L = b^2 \cos^2\phi + a^2 \sin^2\phi$
$M = OA \sin\eta \, (b^2 \cos\phi \cos\zeta + a^2 \sin\phi \sin\zeta)$
$N = (OA \sin\eta)^2 (b^2 \cos^2\zeta + a^2 \sin^2\zeta) - a^2 b^2 [1 - (B_b - c)^2/c^2].$

References

Amin, B. S., Lal, D., Lorin, J. C., Pellas, P., Rajan, R. S., Tamhane, A. S., and Venkatavaradan, V. S., 1969: in P. M. Millman (ed.), *Meteorite Research*, D. Reidel Publ. Co., Dordrecht, p. 316.

Arnold, J. R., Honda, M. and Lal, D.: 1961, *J. Geophys. Res.* **66**, 3519.

Bhandari, N., Goswami, J. N., Gupta, S. K., Lal, D., Tamhane, A. S., and Venkatavaradan, V. S.: 1972, in *Proc. Third Lunar Sci. Conf., Geochim. Cosmochim. Acta* **3**, 2811.

Bhandari *et al.*: 1973, to be published.

Biswas, S. and Fichtel, C. E.: 1965, *Space Sci. Rev.* **4**, 709.

Comstock, G. M.: 1972, in S. K. Runcorn and H. C. Urey (eds.), 'The Moon', IAU Symp. **47**, 330.

Crozaz, G., Haack, U., Hair, M., Maurette, M., Walker, R., and Woolum, D.: 1970, in *Proc. First Lunar Sci. Conf., Geochim. Cosmochim. Acta* **3**, 2051.

Crozaz, G., Walker, R., and Woolum, D.: 1971, in *Proc. Second Lunar Sci. Conf., Geochim. Cosmochim. Acta* **3**, 2543.

Durgaprasad, N.: 1964, Thesis, Univ. of Bombay.

Finkel, R. C., Arnold, J. R., Imamura, M., Reedy, R. C., Fruchter, J. S., Loosli, H. H., Evans, J. C., Delany, A. C., and Shedlovsky, J. P.: 1971, in *Proc. Second Lunar Sci. Conf., Geochim. Cosmochim. Acta* **2**, 1773.

Fleischer, R. L., Price, P. B., Walker, R. M., and Maurette, M.: 1967, *J. Geophys. Res.* **72**, 331.

Fleischer, R. L., Haines, E. L., Hart, H. R. Jr., Woods, R. T., and Comstock, G. M.: 1970, in *Proc. Apollo 11 Lunar Sci. Conf., Geochim. Cosmochim. Acta* **3**, 2103.

Henke, R. P. and Benton, E. V.: 1967, Report USNRDL-TR-67-122.

Kohman, T. P. and Bender, M. L.: 1967, in B. S. P. Shen (ed.), *High Energy Nuclear Reaction in Astrophysics*, Benjamin, New York, p. 169.

Lal, D.: 1972, *Space Sci. Rev.* **14**, 3.

Lal, D. and Rajan, R. S.: 1969, *Nature* **223**, 5203, 269.

Lal, D. and Venkatavaradan, V. S.: 1967, *Earth Planet. Sci. Letters* **3**, 299.

Lal, D., Rajan, R. S., and Venkatavaradan, V. S.: 1967, *Geochim. Cosmochim. Acta* **31**, 1959.

Lal, D., Lorin, J. C., Pellas, P., Rajan, R. S., and Tamhane, A. S.: 1969, in P. M. Millman (ed.), *Meteorite Research*, D. Reidel Publ. Co., Dordrecht, Holland, p. 286.

Lal, D., McDougall, D., Wilkening, L., and Arrhenius, G.: 1970, in *Proc. Apollo 11 Lunar Sci. Conf.*, *Geochim. Cosmochim. Acta* **3**, 2295.

Lavrukhina, A. K., Ustinova, G. K., Ibarev, T. A., and Kunznetsova, R. I.: 1969, in P. M. Millman (ed.), *Meteorite Research*, D. Reidel Publ. Co., Dordrecht-Holland, p. 227.

Maurette, M., Thro, P., Walker, R. M., and Webbink, R.: 1969, in P. M. Millman (ed.), *Meteorite Research*, D. Reidel Publ. Co., Dordrecht, Holland, p. 275.

Pellas, P., Poupeau, G., Lorin, J. C., Reeves, H., and Adouze, J.: 1969, *Nature* **223**, 272.

Price, P. B. and O'Sullivan, D.: 1970, in *Proc. First Lunar Sci. Conf.*, *Geochim. Cosmochim. Acta* **3**, 2351.

Price, P. B., Rajan, R. S., and Tamhane, A. S.: 1967, *J. Geophys. Res.* **72**, 1377.

Price, P. B., Hutcheon, I., Cowsik, R., and Barber, D. J.: 1971, *Phys. Rev. Letters* **26**, 916.

Reedy, R. C. and Arnold, J. R.: 1972, *J. Geophys. Res.* **77**, 537.

Rudstam, G.: 1956, Thesis, Univ. of Uppsala.

Shapiro, M. M. and Silberberg, R.: 1970, *Ann. Rev. Nucl. Sci.* **20**, 323.

Shedlovsky, J. P., Honda, M., Reedy, R. C., Evans, J. C. Jr., Lal, D., Lindstrom, R. M., Delany, A. C., Arnold, J. R., Loosi, H. H., Fruchter, J. S., and Finkel, R. C.: 1970, in *Proc. First Lunar Sci. Conf.*, *Geochim. Cosmochim. Acta* **2**, 1503.

Tamhane, A. S.: 1972, Thesis, Univ. of Bombay.

Tanaka, S., Sakamoto, K., and Komura, K.: 1972, *J. Geophys. Res.* **77**, 4281.

Venkatavaradan, V. S.: 1970, Thesis, Univ. of Bombay.

Waddington, C. J.: 1960, *Phil. Mag.* **5**, 311.

Wahlen, M., Honda, M., Imamura, M., Fruchter, J., Finckel, R., Kohl, C., Arnold, J., and Reedy, R.: 1972, 'Revised Abstracts', *Third Lunar Sci. Conf.* (ed. by C. Watkins), p. 764.